A Numerical Study on the Keyhole Formation During Laser Powder Bed Fusion Process

Subin Shrestha[1]
J.B. Speed School of Engineering,
University of Louisville,
Louisville, KY 40292
e-mail: subin.shrestha@louisville.edu

Y. Kevin Chou
J.B. Speed School of Engineering,
University of Louisville,
Louisville, KY 40292
e-mail: kevin.chou@louisville.edu

The dynamic phenomenon of a melt pool during the laser powder bed fusion (LPBF) process is complex and sensitive to process parameters. As the energy density input exceeds a certain threshold, a huge vapor depression may form, known as the keyhole. This study focuses on understanding the keyhole behavior and related pore formation during the LPBF process through numerical analysis. For this purpose, a thermo-fluid model with discrete powder particles is developed. The powder distribution, obtained from a discrete element method (DEM), is incorporated into the computational domain to develop a 3D process physics model using FLOW-3D. The melt pool formation during the conduction mode and the keyhole mode of melting has been discerned and explained. The high energy density leads to the formation of a vapor column and consequently pores under the laser scan track. Further, the keyhole shape resulted from different laser powers and scan speeds is investigated. The numerical results indicated that the keyhole size increases with the increase in the laser power even with the same energy density. The keyhole becomes stable at a higher power, which may reduce the occurrence of pores during laser scanning. [DOI: 10.1115/1.4044100]

Keywords: additive manufacturing, keyhole, laser powder bed fusion, porosity

1 Introduction

Laser powder bed fusion (LPBF) process is a metal-based additive manufacturing (AM) technology, which utilizes a laser to sequentially melt the powder particles. Due to the line-by-line and layer-by-layer scanning process, complex geometries can be fabricated using LPBF. However, the process itself would induce defects due to high thermal gradient and residual heats [1]. The severity of defects formation depends upon the process parameters, and hence, the proper selection of process parameters is a must.

Several studies have been carried out to find the optimum process window that would give full density parts [2,3]. Single-track experiment would provide knowledge about the track profile, mode of melting, etc. However, it would require build preparations, part fabrication, metallography, etc., to get all the information that is costly as well as time-consuming. Hence, predictive simulation models in LPBF are very important as it would reduce the experimental efforts. In addition, simulation tools also help to understand the underlying physical phenomenon that is otherwise difficult to observe from experiments [4].

The melt pool behavior during the single-track formation depends on the process parameters selected such as laser power and scan speed [5]. Furthermore, the surface quality of the layer would additionally depend on the hatch spacing [6]. Lee and Zhang [7] developed a high-fidelity numerical model by including physics such as the Marangoni effect and recoil pressure, which are important to correctly predict the melt flow during the selective laser melting (SLM) process. The recoil pressure due to evaporation causes significant depression, and its inclusion within the model helps predict melt pool depth accurately. In addition, the transverse cross-section profile of the molten pool was found to be relatively symmetric about the center of the laser. In a similar manner, Wu et al. [8] demonstrated that the recoil pressure triggered keyhole formation significantly affects the flow behavior, which in turn affects the track morphology. Melt pool predicted with recoil pressure is deeper and narrower compared with the identical model without the recoil pressure. Khairallah et al. [9] incorporated a ray tracing laser heat source to predict the heat transfer and fluid flow during the LPBF process. The single-track simulation explained the complex melt flow as well as the formation of pores and denudation zones. Tan et al. [10] utilized the powder scale model to study the evolution of porosity during different modes of melting. It was found that pores formed due to lower energy density were irregular in shape while those formed with high energy density were spherical or elliptical in shapes. Besides, multiphysics model has been applied to compare the melt pool formation between two different materials: steel and molybdenum [11]. The melt pool size predicted for molybdenum is much smaller than steel due to its higher thermal conductivity.

During the LPBF process, pores may form due to incomplete melting known as lack of fusion pores or due to over-melting known as keyhole pores. When the energy density is very high, material evaporation occurs, which leads to the formation of a keyhole. Zhao et al. [12] used ultrafast X-ray imaging for real-time monitoring of the LPBF process. The static laser source applied to the powder bed system shows the development of keyhole and the formation of pore after the laser turn off. Parab et al. [13] captured the transient behavior of the keyhole using high-speed synchrotron X-ray imaging. The keyhole shapes formed during the LPBF of Al-Si10-Mg at Ti-6Al-4V were presented, and the images showed the change in keyhole shape with the change of processing parameters such as laser power and scan speed. Likewise, Cunningham et al. [14] carried out a detail X-ray imaging experiment to observe the keyhole threshold and morphology in laser melting of Ti-6Al-4V alloy. The captured images show the transition from conduction to keyhole mode of melting. The shape and size of vapor depression vary widely across the P-V space. The results also show that the spot size affects the magnitude of vapor depression. These experiments certainly help visualize and understand the powder dynamics, keyhole formation, etc., especially the complexity of the process itself to be fully captured by the simulation. In addition, the micro-CT-based porosity study has shown that within the same line energy density (LED), the porosity level would depend on the power [15]. As the power increased to 140 W at LED of 0.4 J/mm, the pore number increased while there was a drop in the pore number and volume as the power

[1]Corresponding author.

Manuscript received May 7, 2019; final manuscript received May 15, 2019; published online July 31, 2019. Assoc. Editor: Y. Lawrence Yao.

was further increased. It is difficult to explain such results from the experiment only, as the underlying physics is not known; hence, high-fidelity simulation would help understand the keyhole behavior during the LPBF process.

In this study, a powder scale model is developed including complex physics such as Marangoni effect, recoil pressure, evaporation, multiple reflections within keyhole, etc., which are important to predict different modes of melting during the LPBF process. The melt pool predicted at different modes: conduction and keyhole melting were compared and validated against the experiment, and then the effect of power and speed toward the keyhole behavior has been investigated.

2 Discrete Element Method

LPBF is a powder bed AM process. Due to the presence of the porosity between the powders, the laser interaction would be different compared with the flat surface. Ye et al. [16] studied the effect of powder bed thickness on the laser absorptivity, and the results indicated that at low power, the difference in absorptivity is significant. Hence, it is important to model the powder particles as there would be multiple reflections of laser rays inside the powder bed. Discrete element method (DEM) is a numerical scheme developed to simulate the behavior of discrete interacting bodies [17], and therefore, it is a suitable approach to simulate the powder distribution in the LPBF process. An opensource DEM code called LIGGGHTS (LAMMPS Improved for General Granular and Granular Heat Transfer Simulations) is used to simulate the powder distribution process. The powder generation and recoating process of LPBF is simulated by designing a reduced size of the dispenser platform and build platform as shown in Fig. 1. The distribution of the powder diameter with range 0–45 μm is discretized to get the percentage mass distribution. This discretized particle size range is then utilized to generate the powder particles based on the mass

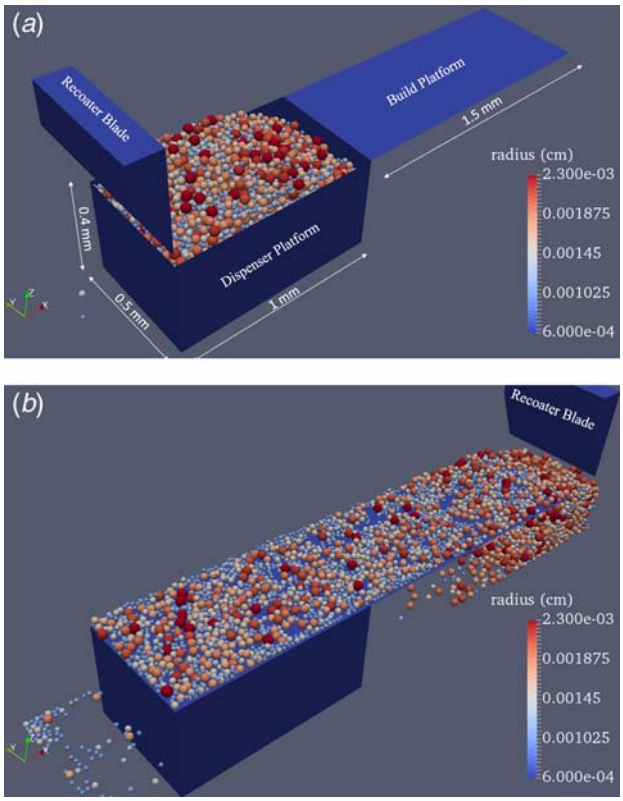

Fig. 1 (*a*) Powder added to the dispenser platform and (*b*) powder particles settled over build plate after the recoating process

contribution. Due to the use of an explicit time integration scheme and small particle diameters, very small time-step size should be used. The time step is chosen which satisfies the Rayleigh criteria shown in Eq. (1) [18]. In order to maintain a reasonable time-step size, the minimum powder radius used is 10 μm

$$\Delta t = \frac{\pi R_{\min}\sqrt{\rho/E}}{0.163v + 0.877} \tag{1}$$

where Δt is the time-step size, $R_{\min}$ is the minimum radius of the powder particles, ρ is the density, E is the modulus of elasticity, and v is the speed of powder. The material properties of Ti-6Al-4V such as modulus of elasticity, poisons ratio, etc., used during the simulation have been summarized in Table 1.

In the DEM algorithm, all particles are identified separately by their radius, mass, moment of inertia, etc., and all the particles are tracked by solving their trajectories. The general forms of model equations are presented (Eqs. (2) and (3)) [19]. The force balance for the particle with index i is

$$m_i\ddot{x}_i = F_{i,n} + F_{i,t} + F_{i,b} \tag{2}$$

$$I_i\frac{\mathrm{d}\omega_i}{\mathrm{d}t} = r_{i,c} \times F_{i,t} + T_{i,r} \tag{3}$$

where $F_{i,n}$ is the normal particle–particle contact force, $F_{i,t}$ is the tangential contact force, and $F_{i,b}$ is the body force (gravity in this case). The torque due to tangential force is given by $r_{i,c} \times F_{i,t}$, while $T_{i,r}$ is an additional torque on the particle modeled by means of a rolling friction. The particle–particle contact models have been explained in detail in Ref. [19].

The spherical powder particles are generated based on the distribution and dropped into the dispenser platform. During the spreading process, there is an interaction between particles and mesh walls in addition to the particle–particle interaction. Figure 1(*a*) shows the randomly distributed powder particles over the dispenser platform. As the powder settles in the platform, it is moved along the positive Z-direction, and the recoater blade is moved toward the build platform. During this process, the interaction between powder particles and build platform determine the powder bed distribution, which is depicted in Fig. 1(*b*). Besides, the powder distribution over the build platform also depends on several factors such as build platform surface, size distribution, and an angle of repose [20]. The distance of 60 μm is maintained between the tip of the blade and the build platform considering the maximum diameter of the particle is 45 μm.

3 Thermo-Fluid Simulation

3.1 Simulation Domain. A 3D thermo-fluid model is developed using a FLOW-3D software as shown in Fig. 2. During the LPBF single-track formation, a laser travels along a line with predefined speed. The width and depth of the melt pool depend on the process parameters used, and the higher energy densities result in a wider and deeper melt pool [21]. As this study is focused on keyhole mode melting, a bigger computational domain along the depth is required. Hence, a 3D model with a domain size of 1200 μm × 400 μm × 520 μm is developed. The powder over the

Table 1 Ti-6Al-4V properties for DEM simulation

Parameters	Values
Density (kg/m^3)	4420
Modulus of elasticity (GPa)	114
Poisson's ratio	0.41
Coefficient of restitution	0.5
Sliding friction coefficient	0.5
Rolling friction coefficient	0.1

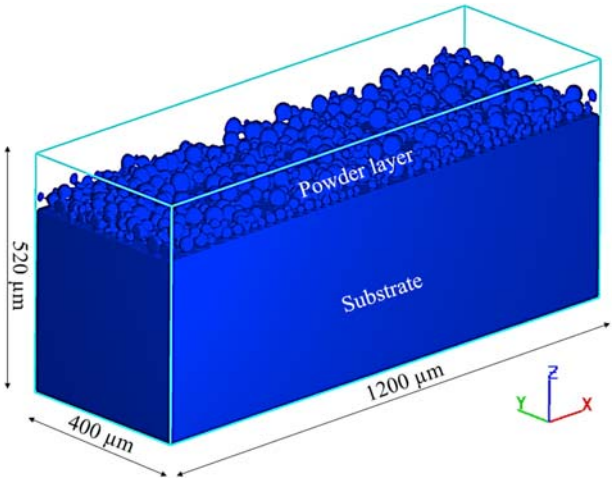

Fig. 2 3D computational domain used for single-track simulation

base platform is imported from the LIGGGHTS simulation result. The domain is represented based on the fluid fraction. Powder and solid have a fluid fraction of 1, and the void has 0 fluid fraction. Since the volume of fluid is used to predict the surface formation, a hexahedral mesh of 5 μm is applied to the computational domain which resulted in 2.1 million cells. In addition, all the walls of the domain are assigned with adiabatic boundary conditions.

During the simulation, the laser was turned on at 200 μm in positive X- and Y-direction, and the total length of 800 μm was scanned. After the laser traveled 800 μm, it was turned off, and the melt pool was let to solidify. The simulated scan length would be enough to investigate the behavior of the keyhole formed due to parameter settings. The scan time of 2 ms took 48 h of computational time with 16 Intel® Xeon® E5-2695 processors.

3.2 Material Properties. The physical properties such as thermal conductivity, specific heat, and density are the function of temperature. Therefore, the temperature-dependent material properties summarized in Fig. 3 are used to define solid and powder Ti-6Al-4V. In addition, other properties are listed in Table 2.

3.3 Boundary Conditions. During the simulation, momentum and energy balance equations are solved to predict the fluid flow and temperature, respectively. The heat input from the laser is modeled as a moving Gaussian distribution heat source in the horizontal direction and the equation of the source is presented in Eq. (4),

$$q(w) = \frac{2aP}{\pi r^2}\exp\left(-\frac{2w^2}{r^2}\right) \tag{4}$$

where q is the heat flux at a radial distance w from beam center, P is laser power, a is absorptivity of the material based on Fresnel reflection, and r is the laser beam radius.

As the heat source is applied, the temperature of the powder and substrate increases and the powder begin to melt. When the melting point is reached, the flow is primarily governed by the surface tension which is defined by

$$\gamma = \gamma_m + \frac{\mathrm{d}\gamma}{\mathrm{d}T}\Delta T \tag{5}$$

where γ is the surface tension, γ_m is the surface tension at the melting point, $\mathrm{d}\gamma/\mathrm{d}T$ is the surface tension gradient, and ΔT is the temperature difference. Metals generally have negative surface tension gradient, and therefore, melt flow occurs from higher temperature region to lower temperature region. Due to the melt flow, the surface deforms with time, and the deformed surface is captured

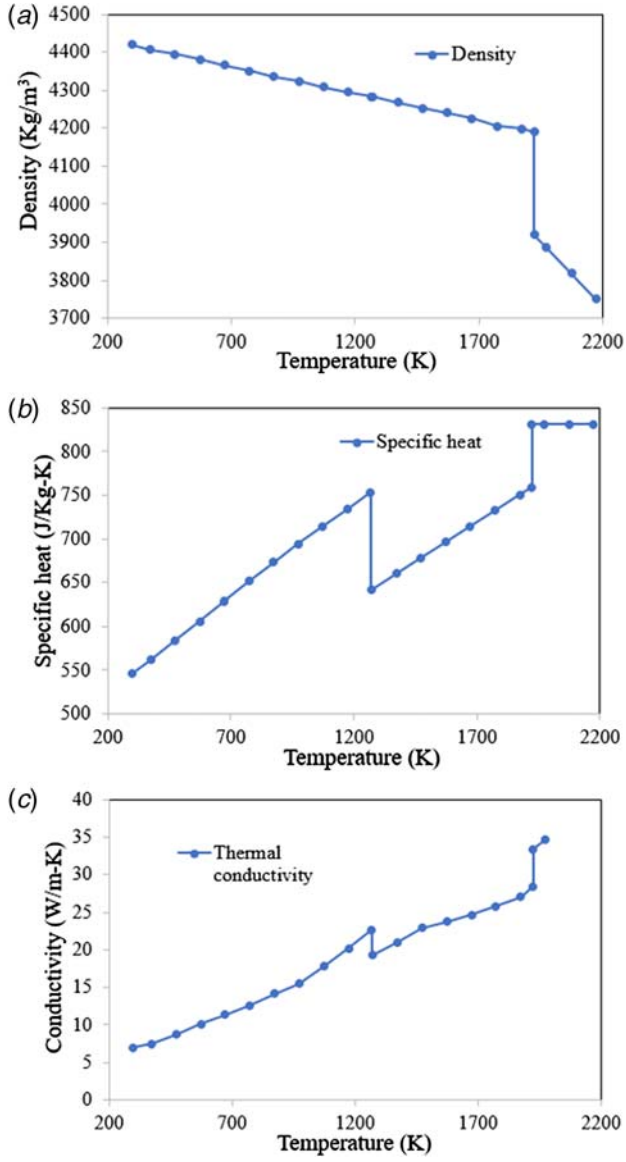

Fig. 3 Temperature-dependent material properties of Ti-6Al-4V [22]

by updating the fluid fraction using Eq. (6) [23]

$$\frac{\partial F}{\partial t} + (V.\nabla)F = 0 \tag{6}$$

In addition, when the temperature within the melt pool exceeds the boiling temperature, metal evaporation occurs leading to recoil pressure. The pressure boundary condition used in the

Table 2 Properties of Ti-6Al-4V in a thermo-fluid simulation

Parameters	Values
Solidus temperature, T_S (K)	1878
Liquidus temperature, T_L (K)	1928
Boiling temperature, T_v (K)	3533
Latent heat of fusion, L_f (kJ/kg)	286
Latent heat of evaporation (kJ/kg)	9830
Viscosity (kg/m s)	0.005
Surface tension (N/m)	1.68
Surface tension gradient (N/m K)	−0.00026

simulation is [24]

$$P_{\text{recoil}} = 0.54 P_0 \exp\left(\frac{\Delta H_v (T - T_v)}{RTT_v}\right) \tag{7}$$

where P_0 is the atmospheric pressure, ΔH_v is the specific enthalpy of metal vapor, T_v is the boiling temperature, T is the surface temperature, and R is the universal gas constant. Equation (7) can be simplified as

$$Ps = A \ \exp\left\{B\left(1 - \frac{Tv}{T}\right)\right\} \tag{8}$$

where $A = 0.54 * P_0$ and B is a coefficient that is the ratio of latent heat of evaporation to a product of the gas constant and T_v.

The recoil pressure or evaporation pressure would increase the melt pool depth due to the formation of vapor depression, which may lead to keyhole formation depending upon the magnitude of the material evaporation. The vapor formation would change the absorptivity within the keyhole as vapor has a different rate of absorption than the molten metal. Also, within this keyhole, multiple reflections of the laser occur from the keyhole walls, which have been approximated by Fresnel reflection as

$$a = 1 - \frac{1}{2}\left(\frac{1 + (1 - \varepsilon \cos\phi)^2}{1 + (1 + \varepsilon \cos\phi)^2} + \frac{\varepsilon^2 - 2\varepsilon \cos\phi + 2\cos^2\phi}{\varepsilon^2 + 2\varepsilon \cos\phi + 2\cos^2\phi}\right) \tag{9}$$

where ϕ is the angle between the incident ray and the surface normal, ε depends on material properties and laser type and is related to electrical conductance per unit depth (σ_{st}) of metal, the real part of the dielectric constants (ε_1, ε_2), and the permittivity of vacuum (ε_o), and ω represent the angular frequency that is one of the laser properties [24]

$$\varepsilon^2 = \frac{2\varepsilon_2}{\varepsilon_1 + \left[\varepsilon_1^2 + \left(\frac{\sigma_{st}}{\omega \varepsilon_o}\right)^2\right]^{1/2}} \tag{10}$$

4 Results and Discussion

4.1 Typical Simulation Result. During the LPBF process, the selection of process parameters would determine the melt behavior. Depending upon the laser power and scan speed, incomplete melting, conduction mode melting, and keyhole mode melting are possible. The following sections discuss the melt pool behavior and the significance of different physics during the conduction mode and the keyhole mode of melting. The melt pool cross sections have been compared with the experimental results from the literature [21,25].

4.1.1 Conduction Mode. In this case, the laser power of 195 W and a scan speed of 1000 mm/s is used. Since the melt pool penetration would not be high, the substrate size was reduced, and 200 μm thick substrate is used only for this case. Figure 4 presents the temperature distribution and the melt flow during laser motion. The figure shows the melt pool while the laser is still in motion and the velocity is maximum at the laser application area, which gradually decreases toward the solidification front. Also, the melt pool gradually solidifies as the laser beam moves further away.

Depression is observed at the laser application area which is due to the recoil pressure. But, the recoil pressure at this setup is not enough to develop a keyhole, and therefore, melt pool is stable. Cunningham et al. [14] performed X-ray imaging during the single-track formation of similar process parameters, which is presented in their supplementary results. The numerical simulation can predict the shape of the depression formed at those parameters.

The simulation melt pool depth is around 70 μm, which suggests that the penetration would be enough to form a strong bond between layers when 30 μm layer thickness is used in the experiment. No pores are observed during 0.8 mm scan length simulation due to the stability of the melt pool. The melt region after the single track has completely formed is shown in Fig. 5. A depressed area is formed at the end of the scan track. Bertoli et al. [26] have explained the transient behavior of the single track at the beginning and end of the scan. Bump is formed at the laser turn-on region and height profile slopes downward at the laser turn off region. Figure 6 compares the simulation result with the experiment carried out with the same processing parameters [25]. A near semi-circular melt pool shape is predicted with the applied parameters, and the melt pool cross-section comparison shows that the simulation can be used to predict the melt pool penetration and boundary during the LPBF process. The melt pool profile is in good agreement with the result of the experiment.

4.1.2 Keyhole Mode. During the keyhole mode melting, the material evaporation leads to a repulsive force within the melt pool and an opening is formed which is filled with the vapor. The evaporation pressure developed would depend on the evaporation flux. This pressure acts to open the keyhole. As the size of the vapor column increases, more vapor is trapped inside it, and the absorption of the keyhole wall further increases. Hence, the depression, as well as the vapor column, continues to grow.

On the other hand, surface tension pressure along with convection-induced pressure and hydrostatic pressure act to close the keyhole. However, the magnitude of convection-induced pressure and hydrostatic pressure could be neglected due to its weak

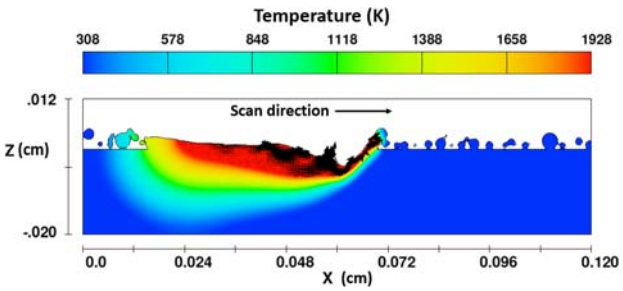

Fig. 4 Powder and substrate melting during laser application

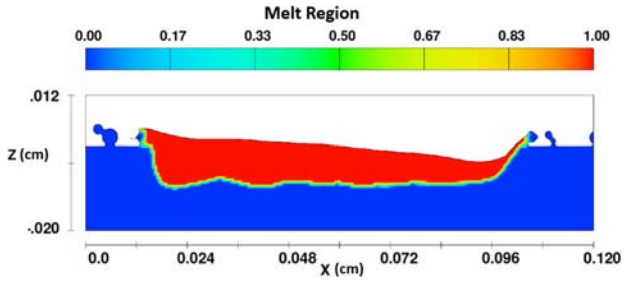

Fig. 5 Melt region formed after complete melting and solidification

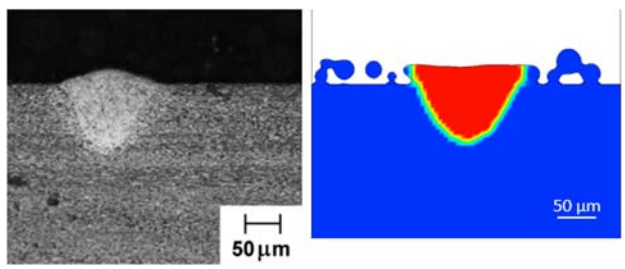

Fig. 6 Melt pool boundary comparison between the experiment [25] and the simulation

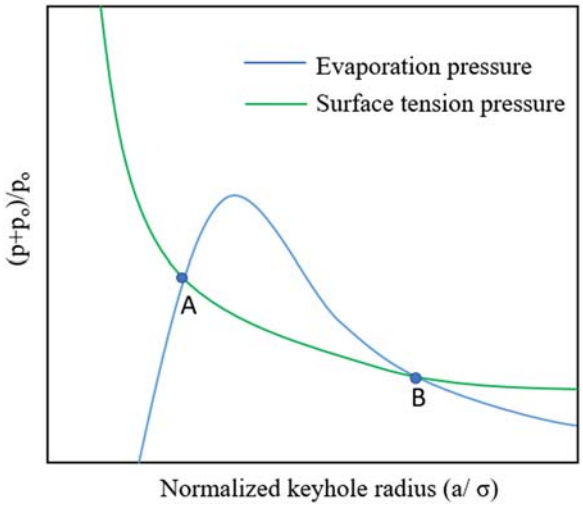

Fig. 7 Equilibrium points during the formation of vapor column [27]

contribution [27]. As the vapor column becomes wider, the tendency of it to collapse due to surface tension becomes less.

Figure 7 shows the relationship between the excess evaporation pressure $((p+p_o)/p_o)$ and the surface tension pressure based on the normalized keyhole radius a/σ [27]. The pressure on the keyhole wall $(p+p_o)$ is normalized with ambient pressure p_o, and the keyhole radius (a) is normalized with laser beam radius σ. The two equilibrium states (A and B) shown in Fig. 8 are obtained from energy and pressure balance equations given in Eqs. (11) and (12), respectively [27].

$$q_{abs} = q_\lambda + q_{abl} \tag{11}$$

$$p_{abl}(a) = p_\Upsilon(a) \tag{12}$$

where q_{abs} is the absorbed energy flux density, q_λ is the heat conduction losses, q_{abl} is the energy carried away by evaporation, $p_{abl}(a)$ is the evaporation pressure, and $p_\Upsilon(a)$ is the surface tension pressure. When the vapor column is below the point A (r_a), the surface tension force can close the vapor column, but if the vapor column continues to grow beyond A, the surface tension force is unable to close the vapor column and the stable keyhole is formed. Due to this, point A is regarded as an unstable equilibrium [27]. As the vapor column continues to grow, at a certain point, another equilibrium can be observed which is represented by point B. This is a stable equilibrium where the surface tension would act dominantly to close the vapor column if it further grows.

A high line energy density has been used to observe the keyhole mode of melting. 195 W laser power and 400 mm/s scan speed are used for this purpose as it would result in pores due to keyhole melting [15]. As the energy density is very high, the temperature within the keyhole exceeds the evaporation temperature, and material evaporation leads to the recoil pressure. Hence, vapor depression is formed, which further enhances the laser absorption due to multiple reflections through the keyhole walls. This causes more vapor to form and keyhole depth increases. Figure 8 presents the formation of the depression, which shows the changing multiple reflections due to the change in the surface morphology. At 20 μs, the penetration is not deep; however, as the material is continuously irradiated with the laser, there is an increase in the depression. During this period, there is a high interaction between evaporation pressure and surface tension. A surface tension force tries to close the vapor gap developed, which can be observed at 140 μs. But, due to the high intensity of the laser, the keyhole remains open during most of the melting process. However, the keyhole closes as the vapor column reaches close to the equilibrium. Due to this, pores are formed, and some of them are trapped in the solidification front.

Figure 9 illustrates the formation of pore during the keyhole mode melting. Figure 9(*a*) shows the transient keyhole behavior. At 300 μs, the keyhole formed remains open, and with the further development of the keyhole, the surface tension force becomes dominant over the evaporation pressure and the flow tends to close the vapor column. When the force is enough to break the column, a bubble is formed as seen at 360 μs, with strong velocity field around the bubble. These bubbles are either trapped in the solidification front or they collapse. At 390 μs, the bubble has collapsed to the advancing keyhole. The numerical model is able to capture the essence of the keyhole as well as bubble formation in regard to the high-speed X-ray images discussed in the literature [14,28]. Figure 9(*b*) shows the temperature distribution and shape of the vapor depression. The keyhole wall temperature exceeds the evaporation temperature. This suggests that there is continuous evaporation of metal. Due to the formation of vapor column, substantial displacement of liquid from the center of the spot occurs and the liquid moves to the melt pool away from the laser center. Due to this, a surface wave is formed at the rear of the melt pool since the flow is dominant toward the keyhole rear wall. The formation of the surface wave would play a detrimental role in the morphology of the single track. A bubble trapped at the solidification front is also identified. The bubbles which are trapped are the pores that remain within the single track after it is fully formed.

The formation of the transverse profile of the melt pool is explained with Fig. 10. At 260 μs, when the laser is right on top, a depression is formed, which continues to grow (300 μs). As the laser beam moves away, the melt flow is inward which tend to close the depression as seen in 330 μs. After some time, a fully solidified transverse keyhole profile is obtained. The simulated keyhole profile has been compared with the experimental result from the literature in Fig. 11 [21]. The developed numerical model can predict the keyhole shape formed due to high energy density. The transverse profile is in good agreement with the experimental transverse profile.

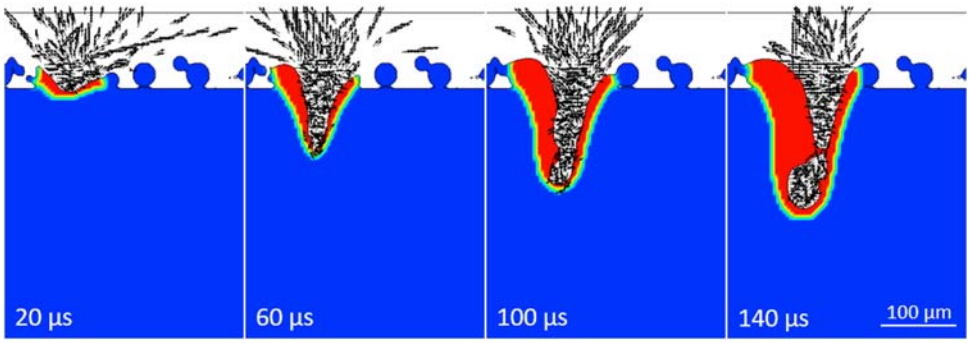

Fig. 8 Multiple reflection vectors from the keyhole wall

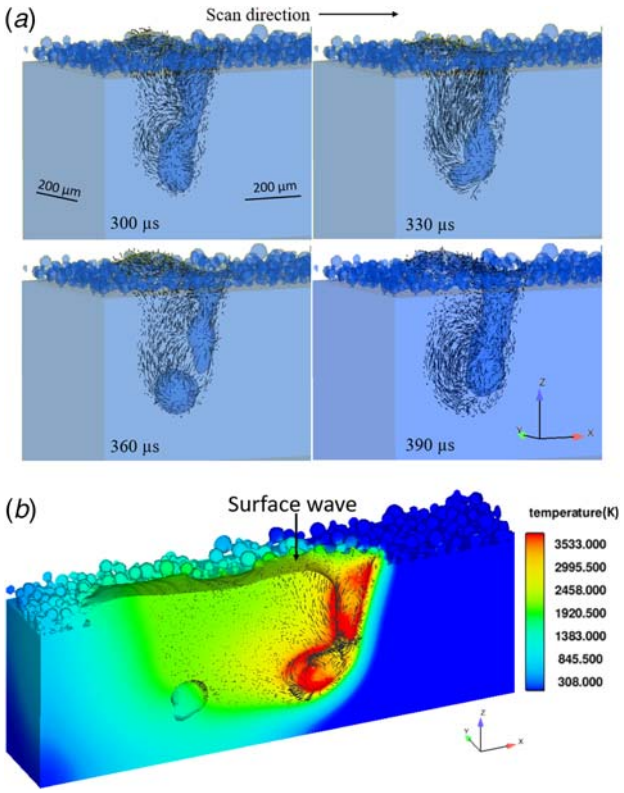

Fig. 9 (*a*) Velocity field, keyhole profile, and breakage of the keyhole to form bubble and (*b*) 2D temperature and velocity field along the longitudinal section

The final single track after solidification is shown in Fig. 12. Several pores are observed within the tracks. These are the pores that were trapped within the solidified melt region. This suggests that the keyhole pores are formed when the process parameters resulting in high energy density is used.

A single-track experiment with the same laser parameters had been carried out using the EOS M270 LPBF system [15]. Ti-6Al-4V powder (0–45 μm) was used to form a 12-mm long single track, and micro-CT was carried out to observe the pores formed within the single track. Figure 13 shows the cross-section

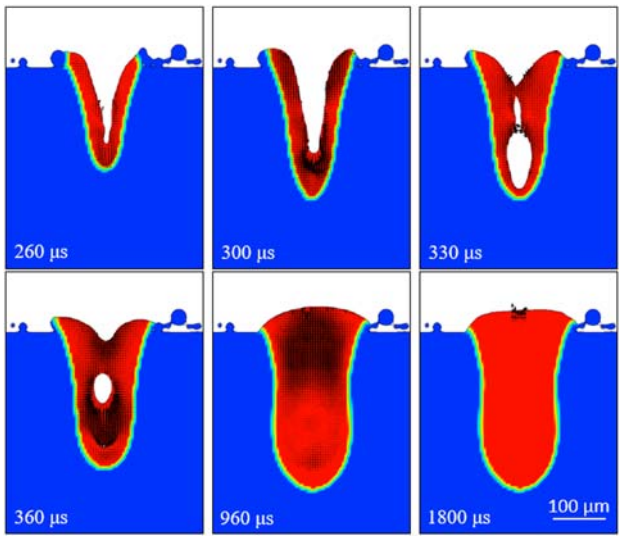

Fig. 10 Fluid flow in the transverse direction during keyhole melting

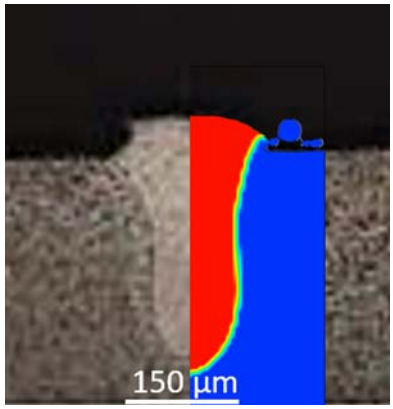

Fig. 11 Melt pool boundary compared with the experiment [21] for 195 W laser power and 400 mm/s scan speed

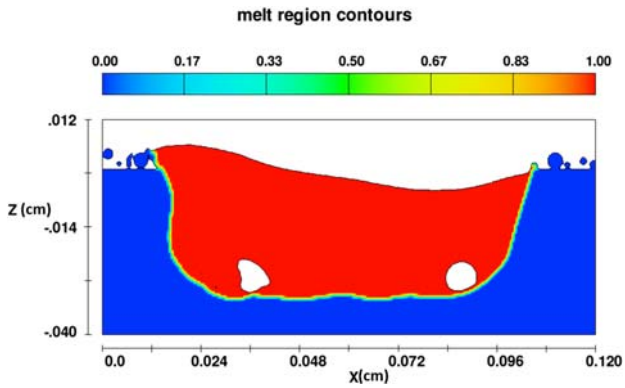

Fig. 12 Melt region formed after complete melting and solidification

Fig. 13 2D images of the pores formed at the beginning of the single track and their 3D-rendered morphology

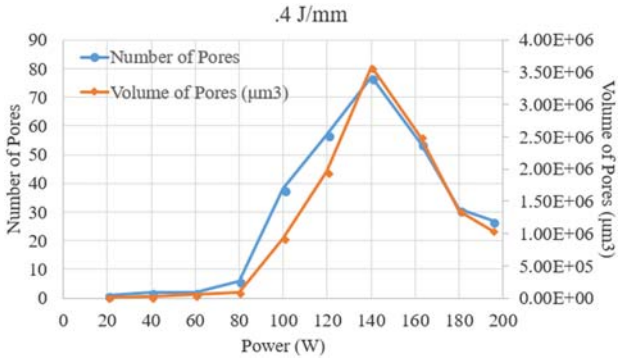

Fig. 14 Pore number and volume from a different level of power with LED = 0.4 J/mm [29]

Table 3 Power and speed with LED = 0.4 J/mm

	LED = 0.4 J/mm			
Power (W)	100	200	300	400
Scan speed (mm/s)	250	500	750	1000

as well as 3D-rendered pores formed at the beginning 3 mm of a single track. Within this region presented, ten keyhole pores are observed.

4.2 Effect of Power and Speed on Keyhole Formation. Line energy density (LED) is the function of laser power (P) and scan speed (v).

$$\text{LED} = \frac{P}{v} \tag{13}$$

At the same energy density, the behavior of the flow and single track would depend upon the power and speed. The range of optimum scan speed varies with the level of power [5]. An experimental study had been carried out to investigate the effect of power and speed on the level of porosity during the formation of 12 mm long single tracks [29]. Figure 14 presents the pore number and pore volume resulting from the different combination of power and speed with an LED of 0.4 J/mm. The results indicated that the pore number and the pore volume increased to a certain level of power and then dropped with a further increase in power at the

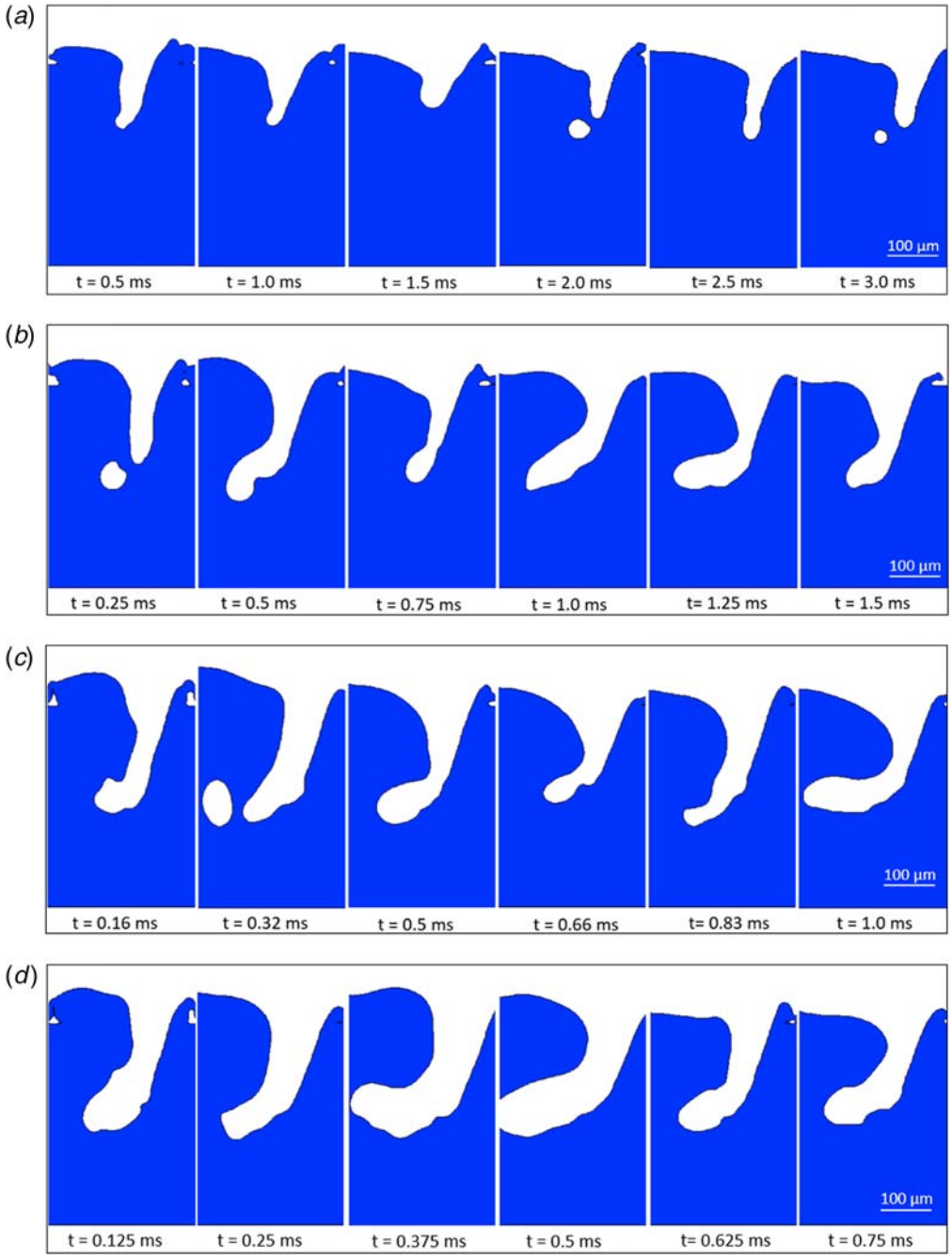

Fig. 15 Keyhole shape at different time steps from different parameters: (*a*) $P = 100$ W, $v = 250$ mm/s, (*b*) $P = 200$ W, $v = 500$ mm/s, (c) $P = 300$ W, $v = 750$ mm/s, and (*d*) $P = 400$ W, $v = 1000$ mm/s

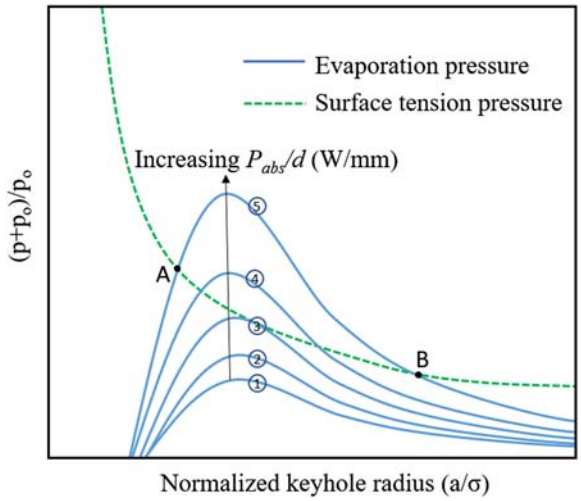

Fig. 16 Intensity dependence in the relationship between vapor column and evaporation pressure [27]

same energy density. This interesting behavior is difficult to explain with experimental study alone, and therefore, the developed numerical model has been utilized to understand the physics that leads to such behavior.

Again, LED of 0.4 J/mm was used for numerical study, which would result in the formation of a keyhole, and the corresponding power and scan speed have been listed in Table 3. The range of laser power is increased to gain more insight toward the keyhole mode melting as the power used in the experiment was limited to 195 W.

Figure 15 displays the keyhole shapes when the laser has moved 0.125 mm, 0.25 mm, 0.375 mm, 0.5 mm, 0.675 mm, and 0.75 mm. The respective times, which would vary with scan speed, have been shown in the figure. The behavior of the keyhole changes with a change in process parameters. For a lower power (100 W) and speed (250 mm/s), the keyhole opening is rather small as shown in Fig. 15(*a*). The keyhole opening increased with an increase in power and speed. For higher power (400 W) and speed (1000 mm/s), the keyhole opening is larger in diameter and the closing force is not enough due to which keyhole remains open for a longer time. In addition, the depth of the penetration is

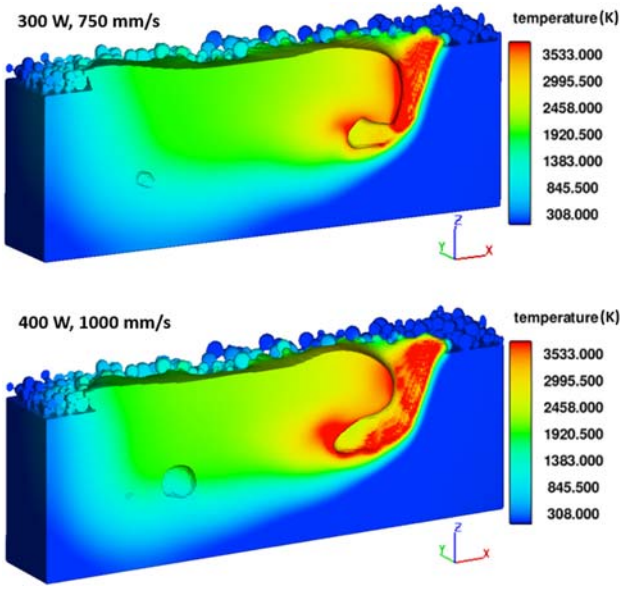

Fig. 17 Temperature distribution when laser has moved 0.8 mm with $P = 300$ W, $v = 750$ mm/s and $P = 400$ W, $v = 1000$ mm/s

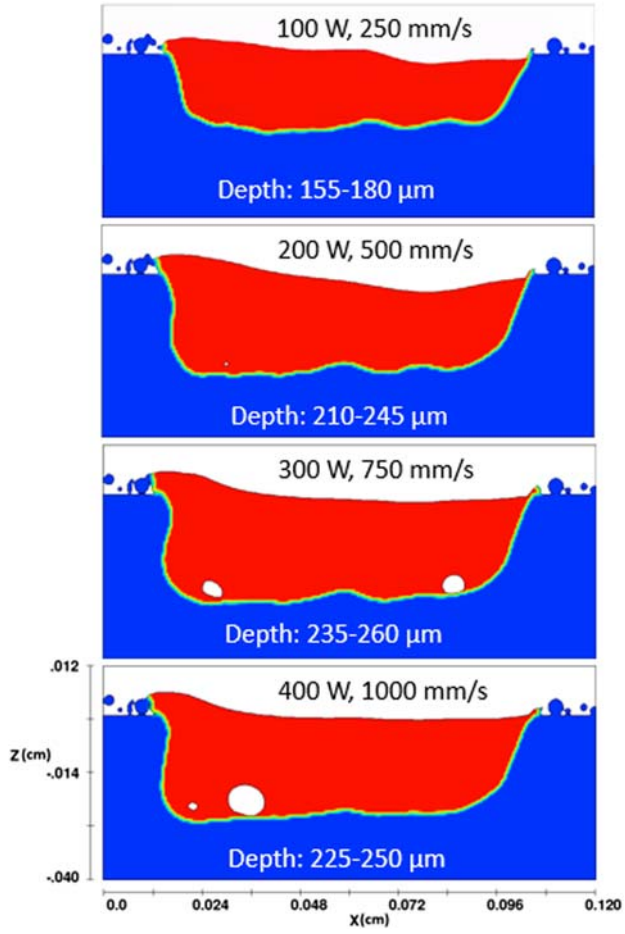

Fig. 18 Melt region with different level of power with LED of 0.4 J/mm

lower for lower power and speed. This behavior may be explained with the expression shown in Eq. (14), which shows that the melt pool depth is more affected by the laser power than the scan speed. The nondimensional depth (δ^*) of the melt pool (ratio of depth to the beam diameter) takes the form [30]

$$\delta^* = fn\left(\frac{ACP}{\rho h_s \sqrt{Dv\sigma^3}}\right) \tag{14}$$

where C is a constant with no dimension and h_s is enthalpy at melting. The 100 W laser power leads to very small vapor opening due to lower intensity while 400 W power leads to higher vapor opening and higher melt pool depth.

Besides, the interaction between evaporation pressure and surface tension is different for different laser power and scan speed. When the intensity is not enough, the equilibrium state is nonexistent, which represents the conduction mode of melting. As the intensity keeps on increasing, deep penetration is observed, and after some point, there exist equilibrium states that decide the stability of the keyhole melt pool as shown in Fig. 16 [27]. The keyhole front wall becomes more inclined with increasing laser power and scan speed.

Figure 17 shows the temperature distribution during laser melting when the power and speed of 300 W and 500 mm/s and 400 W and 1000 mm/s, respectively, are used. The temperature of the melt pool exceeds the evaporation temperature; therefore, the material evaporation occurs at the keyhole walls. However, the keyhole opening is different for these two cases. In this regard, the evaporation pressure effect for two cases would be different and hence the evaporation pressure and surface tension pressure interaction.

Figure 18 exhibits the melt pool boundary formed after solidification. The pores trapped within the melt pool are also identified.

The melt pool depth increased with increasing power from 100 W to 300 W; however, there is a drop in the melt pool depth, when the power is further increased from 300 W to 400 W. This may be due to the change in absorptivity within the melt pool. At some point, when the vapor column exceeds the beam diameter, the absorptivity of the melt pool remains constant, which would explain the reduction of the melt pool depth as speed is also increased along with power. Trapp et al. [31] have performed an experiment to measure the absorptivity of metallic powders during the LPBF process. It was observed that the absorptivity of melt pool increases with the increase in power due to keyhole formation; however, the absorption finally saturates and remains constant on further increase in power. In addition, as the keyhole wall became more inclined with increasing power and speed, the final melt pool shape is also affected by this.

5 Conclusions

A 3D thermo-fluid model has been developed to simulate the LPBF process and investigate the keyhole behavior and pore formation. DEM was used to simulate the particle distribution in a powder bed, and the output was exported as a domain for the thermo-fluid simulation model. A moving Gaussian heat source, surface tension gradient, and evaporation pressure along with multiple reflections within a keyhole were included to predict the melt pool and keyhole behavior. The melt pool results with both conduction and keyhole mode melting have been compared with the experiments from the literature; the melt pool shape and size from the transverse cross-section show a reasonable agreement. As to the keyhole formation in LPBF, its stability strongly depends on the process parameters used. Following are the major findings derived from this study:

- In conduction mode melting, the applied energy is lower with only small depression formed in the melt track. There is no significant interaction between the surface tension pressure and the evaporation pressure in such cases, and thus, no pores were observed.
- In keyhole mode melting, the radius of the keyhole is a strong function of the laser power, and therefore, the keyhole behavior changes with the laser power even at the same energy density. The size of the keyhole radius and its instability determines the frequency of bubble formation within the melt pool.
- The keyhole depth increased with an increase in the laser power from 100 W to 300 W, but then slightly decreased when the power was further increased from 300 W to 400 W, possibly due to the saturation of the laser energy absorption within the keyhole.

Acknowledgment

This research is partially supported by NSF, Manufacturing Machines and Equipment Program (Award # 1662662; Funder ID: 10.13039/100000001).

References

[1] Bauereiß, A., Scharowsky, T., and Körner, C., 2014, "Defect Generation and Propagation Mechanism During Additive Manufacturing by Selective Beam Melting," J. Mater. Process. Technol., **214**(11), pp. 2522–2528.
[2] Gong, H., Rafi, K., Gu, H., Starr, T., and Stucker, B., 2014, "Analysis of Defect Generation in Ti–6Al–4V Parts Made Using Powder Bed Fusion Additive Manufacturing Processes," Add. Manuf., **1**(2014), pp. 87–98.
[3] Wang, Y., Kamath, C., Voisin, T., and Li, Z., 2018, "A Processing Diagram for High-Density Ti-6Al-4V by Selective Laser Melting," Rapid Prototyping J., **24**(9), pp. 1469–1478.
[4] Khairallah, S. A., and Anderson, A., 2014, "Mesoscopic Simulation Model of Selective Laser Melting of Stainless Steel Powder," J. Mater. Process. Technol., **214**(11), pp. 2627–2636.
[5] Yadroitsev, I., Gusarov, A., Yadroitsava, I., and Smurov, I., 2010, "Single Track Formation in Selective Laser Melting of Metal Powders," J. Mater. Process. Technol., **210**(12), pp. 1624–1631.
[6] Xia, M., Gu, D., Yu, G., Dai, D., Chen, H., and Shi, Q., 2016, "Influence of Hatch Spacing on Heat and Mass Transfer, Thermodynamics and Laser Processability During Additive Manufacturing of Inconel 718 Alloy," Int. J. Mach. Tools Manuf., **109**(2016), pp. 147–157.
[7] Lee, Y., and Zhang, W., 2016, "Modeling of Heat Transfer, Fluid Flow and Solidification Microstructure of Nickel-Base Superalloy Fabricated by Laser Powder bed Fusion," Add. Manuf., **12**(2016), pp. 178–188.
[8] Wu, Y.-C., San, C.-H., Chang, C.-H., Lin, H.-J., Marwan, R., Baba, S., and Hwang, W.-S., 2018, "Numerical Modeling of Melt-Pool Behavior in Selective Laser Melting with Random Powder Distribution and Experimental Validation," J. Mater. Process. Technol., **254**(2018), pp. 72–78.
[9] Khairallah, S. A., Anderson, A. T., Rubenchik, A., and King, W. E., 2016, "Laser Powder-bed Fusion Additive Manufacturing: Physics of Complex Melt Flow and Formation Mechanisms of Pores, Spatter, and Denudation Zones," Acta Materialia, **108**(2016), pp. 36–45.
[10] Tan, J., Tang, C., and Wong, C., 2018, "A Computational Study on Porosity Evolution in Parts Produced by Selective Laser Melting," Metall. Mater. Trans. A, **49A**(8), pp. 3663–3673.
[11] Leitz, K.-H., Singer, P., Plankensteiner, A., Tabernig, B., Kestler, H., and Sigl, L. J. M. P. R., 2017, "Multi-Physical Simulation of Selective Laser Melting," Metal Powder Report, **72**(5), pp. 331–338.
[12] Zhao, C., Fezzaa, K., Cunningham, R. W., Wen, H., Carlo, F., Chen, L., Rollett, A. D., and Sun, T., 2017, "Real-time Monitoring of Laser Powder Bed Fusion Process Using High-Speed X-ray Imaging and Diffraction," Sci. Rep., **7**(1), p. 3602.
[13] Parab, N. D., Zhao, C., Cunningham, R., Escano, L. I., Fezzaa, K., Everhart, W., Rollett, A. D., Chen, L., and Sun, T., 2018, "Ultrafast X-ray Imaging of Laser–Metal Additive Manufacturing Processes," J. Synchrotron Radiat., **25**(5), pp. 1467–1477.
[14] Cunningham, R., Zhao, C., Parab, N., Kantzos, C., Pauza, J., Fezzaa, K., Sun, T., and Rollett, A. D., 2019, "Keyhole Threshold and Morphology in Laser Melting Revealed by Ultrahigh-Speed X-Ray Imaging," Science, **363**(6429), pp. 849–852.
[15] Shrestha, S., Starr, T., and Chou, K., 2019, "A Study of Keyhole Porosity in Selective Laser Melting: Single Track Scanning With Micro-CT Analysis," ASME J. Manuf. Sci. Eng., **141**(7), pp. 1–23.
[16] Ye, J., Rubenchik, A. M., Crumb, M. F., Guss, G., and Matthews, M. J., 2018, "Laser Absorption and Scaling Behavior in Powder Bed Fusion Additive Manufacturing of Metals," Proceedings of the CLEO: Science and Innovations, Optical Society of America, San Jose, CA, May 13–18, Optical Society of America, p. JW2A.117.
[17] Mishra, B., and Rajamani, R. K., 1992, "The Discrete Element Method for the Simulation of Ball Mills," Appl. Math. Modell., **16**(11), pp. 598–604.
[18] Yan, W., Qian, Y., Ge, W., Lin, S., Liu, W. K., Lin, F., and Wagner, G. J., 2018, "Meso-Scale Modeling of Multiple-Layer Fabrication Process in Selective Electron Beam Melting: Inter-Layer/Track Voids Formation," Materials and Design, **141**(2018), pp. 210–219.
[19] Kloss, C., Goniva, C., Hager, A., Amberger, S., and Pirker, S., 2012, "Models, Algorithms and Validation for Opensource DEM and CFD–DEM," Prog. Comput. Fluid Dynam. Int. J., **12**(2–3), pp. 140–152.
[20] Escano, L. I., Parab, N. D., Xiong, L., Guo, Q., Zhao, C., Fezzaa, K., Everhart, W., Sun, T., and Chen, L., 2018, "Revealing Particle-Scale Powder Spreading Dynamics in Powder-Bed-Based Additive Manufacturing Process by High-Speed X-Ray Imaging," Sci. Rep., **8**(1), p. 15079.
[21] Gong, H., Gu, H., Zeng, K., Dilip, J., Pal, D., Stucker, B., Christiansen, D., Beuth, J., and Lewandowski, J. J., 2014, "Melt Pool Characterization for Selective Laser Melting of Ti-6Al-4V Pre-Alloyed Powder," Proceedings of the Solid Freeform Fabrication Symposium, Austin, TX, Aug. 4–6, pp. 256–267.
[22] Mills, K. C., 2002, *Recommended Values of Thermophysical Properties for Selected Commercial Alloys*, Woodhead Publishing, Cambridge, UK.
[23] Shrestha, S., and Chou, K., 2017, "A Build Surface Study of Powder-Bed Electron Beam Additive Manufacturing by 3D Thermo-Fluid Simulation and White-Light Interferometry," Int. J. Mach. Tools Manuf., **121**(2017), pp. 37–49.
[24] Cho, J.-H., and Na, S.-J., 2006, "Implementation of Real-Time Multiple Reflection and Fresnel Absorption of Laser Beam in Keyhole," J. Phys. D: Appl. Phys., **39**(24), p. 5372.
[25] Dilip, J., Zhang, S., Teng, C., Zeng, K., Robinson, C., Pal, D., and Stucker, B., 2017, "Influence of Processing Parameters on the Evolution of Melt Pool, Porosity, and Microstructures in Ti-6Al-4V Alloy Parts Fabricated by Selective Laser Melting," Prog. Add. Manuf., **2**(3), pp. 157–167.
[26] Bertoli, U. S., Wolfer, A. J., Matthews, M. J., Delplanque, J.-P. R., and Schoenung, J. M., 2017, "On the Limitations of Volumetric Energy Density as a Design Parameter for Selective Laser Melting," Mater. Des., **113**(2017), pp. 331–340.
[27] Kroos, J., Gratzke, U., and Simon, G., 1993, "Towards a Self-Consistent Model of the Keyhole in Penetration Laser Beam Welding," J. Phys. D: Appl. Phys., **26**(3), p. 474.
[28] Martin, A., Calta, N., Hammons, J., Khairallah, S., Nielsen, M., Shuttlesworth, R., Sinclair, N., Matthews, M., Jeffries, J., and Willey, T., 2019, "Ultrafast Dynamics of Laser-Metal Interactions in Additive Manufacturing Alloys Captured by In Situ X-Ray Imaging," Mater. Today Adv., **1**(2019), p. 100002.
[29] Shrestha, S., Starr, T., and Chou, K., 2018, "Individual and coupled contributions of laser power and scanning speed towards process-induced porosity in selective laser melting," Proceedings of the Solid Freeform Fabrication Symposium, Austin, TX, Aug. 13–15, pp. 1400–1409.
[30] Hann, D., Iammi, J., and Folkes, J., 2011, "A Simple Methodology for Predicting Laser-Weld Properties From Material and Laser Parameters," J. Phys. D: Appl. Phys., **44**(44), p. 445401.
[31] Trapp, J., Rubenchik, A. M., Guss, G., and Matthews, M. J., 2017, "In Situ Absorptivity Measurements of Metallic Powders During Laser Powder-bed Fusion Additive Manufacturing," Appl. Mat. Today, **9**(2017), pp. 341–349.